Thermodynamics of the Heat-Flux Avalanches at the First-Order Magnetic Transition in Magnetocaloric Materials

Marco Piazzi,[1,*] Cecilia Bennati,[2] and Vittorio Basso[1]

[1]*Istituto Nazionale di Ricerca Metrologica, Strada delle Cacce 91, I-10135 Torino, Italy*
[2]*Istituto dei Materiali per l'Elettronica ed il Magnetismo—Consiglio Nazionale delle Ricerche, Parco Area delle Scienze 37/A, I-43124 Parma, Italy*

(Received 11 July 2017; revised manuscript received 22 September 2017; published 30 October 2017)

We investigate the kinetics of first-order magnetic phase transitions by measuring and modeling the heat-flux avalanches corresponding to the irreversible motion of the phase-boundary interface separating the coexisting low- and high-temperature stable magnetic phases. By means of out-of-equilibrium thermodynamics, we encompass the damping mechanisms of the boundary motion in a phenomenological parameter α_s. By analyzing the time behavior of the heat-flux signals measured on La(Fe-Mn-Si)$_{13}$-H magnetocaloric compounds through Peltier calorimetry temperature scans performed at low rates, we relate the linear rise of the individual avalanches to the intrinsic-damping parameter α_s.

DOI: 10.1103/PhysRevApplied.8.044023

I. INTRODUCTION

Magnetic refrigeration around room temperature is emerging as an environmentally friendly, efficient, and increasingly feasible alternative to the conventional vapor-compression cooling technology [1–5]. The physical effect underlying this technique is the magnetocaloric effect (MCE), corresponding to the magnetic-field-induced isothermal entropy change $\Delta S_{\rm iso}(H)$ and the adiabatic temperature variation $\Delta T_{\rm ad}(H)$ occurring in magnetically ordered solid materials under a varying applied magnetic field H [6,7]. Recently, many results have been achieved in the search for materials showing optimal properties for applications, e.g., first-order magnetostructural transitions finely tunable around room temperature, low thermal hysteresis, high entropy and temperature changes [8–13]. Nevertheless, the practical realization of cooling engines based on active-magnetic-regenerative-refrigeration (AMRR) cycles still suffers from some open issues, mainly dealing with the operation frequency of the devices. Although the design of such devices has been substantially improved by the contributions and proposals of many different research groups [14–32], the operation frequency of AMRR-based engines has been only partially worked out. In Ref. [33], Kuz'min showed that this frequency depends on the characteristic relaxation-time constants related to the thermal conductivity of the solid refrigerant ($\tau_{\rm tc}$), to the viscosity of the heat-exchange fluid ($\tau_{\rm fc}$), and to the magnetic processes occurring in the MCE material during the AMRR cycles ($\tau_{\rm mr}$). The conditions to reduce both $\tau_{\rm tc}$ and $\tau_{\rm fc}$—relating them to the values of two parameters, d_r and d_f, representing the cross sections of the refrigerator channels filled with the MCE material and the heat-exchange fluid, respectively—are known [33]. However, the intrinsic magnetic relaxation process has been neglected, with the assumption that the MCE material magnetizes or demagnetizes itself instantaneously when the applied magnetic field is switched on or off. While this can be valid for ferromagnets, like Gd [34,35], if the eddy currents are negligible, it is not the case for first-order MCE materials, like La(Fe-Si)$_{13}$ [36], Fe_2P-type compounds as (Mn-Fe)$_2$(P-As) [37], and $Gd_5(Si_2Ge_2)$ [38], where the magnetization process takes place through a magnetostructural phase transition.

Many efforts have recently focused on the research about the factors limiting the kinetics in this kind of transition [39–51]. Extrinsic factors, possibly masking the intrinsic effects, were carefully evaluated by Moore *et al.* [39] and Lovell *et al.* [43]. By means of magnetic fields varying in time, they have shown that the demagnetizing fields, the thermal contacts between the sample and the measuring setup, and a limited heat diffusion inside the sample represent strong extrinsic limiting factors that must be accurately taken into account. The role of intrinsic thermally activated processes over energy barriers was studied in Ref. [48]. Such an analysis, based on the Johnson-Mehl-Avrami model [52,53], shows that the phase-boundary growth and motion between the ferro- (FM) and paramagnetic (PM) states in La$(Fe_{0.88}Si_{0.12})_{13}$ compounds is predominantly of the two-dimensional type. However, the study does not give enough evidence that intrinsic thermal-activation effects are the main factors limiting the kinetics since similar results can also be attributed to extrinsic effects, namely, the presence of bad thermal contacts between the sample and the external bath [50]. A step forward on this topic has been made by observing that a system slowly driven through its transition, by varying either the applied magnetic field [41] or the temperature

*Corresponding author.
m.piazzi@inrim.it

[51,54], shows heat-flux signals subdivided in spikelike events characterized by an initial linear rise in time followed by an exponential decay. The appearance of these avalanchelike events is an indication of the fact that the phase transformation most probably takes place as a sequence of nucleation events responsible for the phase-boundary growth, followed by the progressive pinning and depinning of the interface front. Studies on the statistics of the avalanches' size distributions have demonstrated that avalanchelike events close to the critical points may be characterized by power-law behaviors, thus suggesting the absence of characteristic length scales in the phase transition [55,56]. In this case, the knowledge of the power-law exponents allows us to infer many aspects of the physics of the underlying transitions, and this approach has already been successfully applied to certain classes of MCE materials [57,58]. However, a thermodynamic approach for the investigation of the dynamic aspects involved in the avalanche patterns, similar to the one employed in normal ferromagnets to describe the magnetization process [59,60], is missing in the case of MCE systems.

In this paper, we aim at developing an out-of-equilibrium thermodynamic model appropriate for extracting a phenomenological damping coefficient α_s from the analysis of the rise times of the individual heat-flux avalanches experimentally detected. The knowledge of this coefficient is crucial to build up a macroscopic model of the kinetics governing the transitions in MCE materials. The model could possibly be employed to predict the high-frequency behavior of MCE-based cooling devices and to compare these predictions with experimental data obtained by varying the magnetic fields at a high sweep rate of about 10–100 Hz [35,61,62]. In developing the model, we concentrate on the presence of metastable states in the energy landscape of the system and on the factors limiting the velocity of the phase front. In the classical Stefan problem [63–65], the phase front is described at the equilibrium temperature and the heat-diffusion processes limiting its growth are considered. Within this approach, the thermodynamic equilibrium is maintained at the expense of the emergence of strong local temperature gradients. In the present case of solid-solid phase transitions occurring in the MCE materials, we are dealing with metals characterized by a high heat conductivity and a distribution of defects which suggests using an out-of-equilibrium description of the moving front. In this case, the latter is allowed to be at a temperature different from the equilibrium one [66], and the temperature gradients will be relevant only on length scales much larger than the microstructural ones. For this reason, we employ the out-of-equilibrium thermodynamics of linear systems and, on a phenomenological basis, we assume that the velocity of the phase front should be proportional to the distance from equilibrium, with the proportionality coefficient represented by α_s.

In this paper, after deriving the model, we apply it to interpret the time behavior of the heat-flux signals experimentally detected through temperature scans performed at a rate of 1 mK/s and for various applied magnetic fields H on a series of $La(Fe\text{-}Mn\text{-}Si)_{13}\text{-}H_{1.65}$ compounds. From the comparison, we can extract the values of the damping coefficient α_s and of the latent heat of the system Δu_L, finding that, within the uncertainty limits, $\alpha_s/\Delta u_L \approx 0.5 \times 10^{-3}$ $(\mathrm{m/s})\,\mathrm{K}^{-1}$, independent of both H and the material composition. Moreover, we determine the time scales involved in the transition process, showing that the intrinsic damping and the heat exchange with the external thermal bath are governed by time constants having the same order of magnitude.

The paper is organized as follows. In Sec. II, we introduce the out-of-equilibrium thermodynamic theory of linear systems by first describing homogeneous systems (Sec. II A) and then extending out to the case of space-extended macroscopic systems in which phase coexistence occurs (Sec. II B). In Sec. III, we derive first the kinetic constitutive equation of the system from a continuity equation for the energy (Sec. III A). We then apply the above theory to the analysis of solid-state MCE transitions in quasi-isothermal conditions by adding the role of an external thermal reservoir (Sec. III B) and we find the theoretical behavior of the heat flux in the case of individual-avalanche events (Sec. III C). In Sec. IV, we compare the theoretical predictions with the experimental data obtained by Peltier calorimetry temperature scans at a low rate and, in Sec. V, we discuss the results obtained, suggesting also possible routes for future works. Finally, in Sec. VI, we present our conclusions.

II. OUT-OF-EQUILIBRIUM THERMODYNAMICS OF FIRST-ORDER PHASE TRANSITIONS

A. Homogeneous systems

Let us consider to deal with an isotropic magnetic system in which the magnetic moment $\boldsymbol{m}$ and the applied magnetic field $\boldsymbol{H}$ are fixed along an arbitrary direction, so that, in what follows, we can limit to consider their scalar amplitudes m and H, respectively. Such a system is characterized by the entropy S and the magnetic moment m. Since the controlled magnetic variable is the magnetic field H, we can describe the system through the enthalpy potential $U_e(S,H) = U - \mu_0 H m$, where U is the internal energy [67]. A first-order phase transition will be characterized by a nonmonotonic behavior of the equation of state

$$T_p(S,H) = \frac{\partial U_e}{\partial S}, \tag{1}$$

so that the temperature of the system T will not follow everywhere the equilibrium temperature path which is defined by T_p. The typical behavior is depicted in

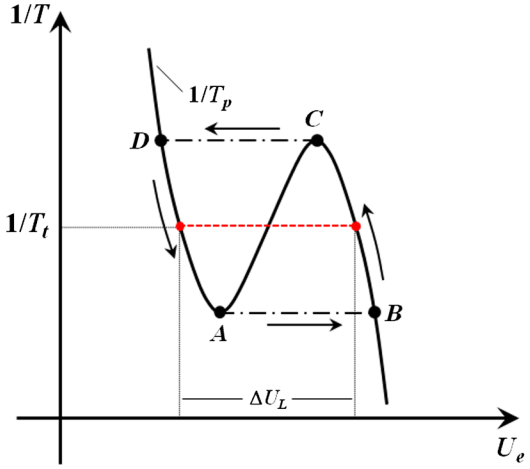

FIG. 1. Out-of-equilibrium first-order transition in homogeneous systems: temperature $1/T_p$ [Eq. (1)] vs enthalpy U_e. Arrows show the path followed by the system upon heating (D-A-B) and subsequent cooling (B-C-D). Dashed-dotted black lines represent the out-of-equilibrium states explored during the transition, after the limits of stability A and C are overcome. $1/T_t$ (the dashed red line) is the equilibrium transition temperature path following the Maxwell construction (see also Fig. 2). ΔU_L is the enthalpy change at T_t, whose volume density Δu_L appears in Eq. (10) and in Table I.

Fig. 1, where we show the out-of-equilibrium path as $1/T_p$ as a function of the enthalpy U_e. Upon heating, after reaching the limit of stability, i.e., point A in Fig. 1, T will pass through a sequence of high-energy out-of-equilibrium states going towards the first available equilibrium state, i.e., point B in Fig. 1. The rate at which T relaxes towards the new equilibrium state should be determined by means of nonequilibrium thermodynamics.

The main observation to take into account is that, when T is in a nonequilibrium state higher than T_p [Eq. (1)], the entropy change per unit time dS/dt is $(1/T_p)\partial U_e/\partial t$, which is higher than $(1/T)\partial U_e/\partial t$. The difference is associated with the presence of internal entropy production processes. Therefore, by describing the internal entropy production processes through the entropy production rate $\Sigma_s \geq 0$, the entropy-change rate reads

$$\frac{dS}{dt} = \frac{1}{T}\frac{dU_e}{dt} + \Sigma_s. \tag{2}$$

From Eqs. (1) and (2), we immediately obtain the following expression for the entropy production rate:

$$\Sigma_s = \left(\frac{1}{T_p} - \frac{1}{T}\right)\frac{dU_e}{dt}. \tag{3}$$

In Eq. (3), we can recognize two different terms. The first one, dU_e/dt, represents the velocity of the relaxation process bringing the system temperature T back to the equilibrium value. The second term, $(1/T_p - 1/T)$, is proportional to the distance of the system temperature T from the equilibrium value T_p. Then, in the framework of out-of-equilibrium thermodynamics of linear systems, the latter term acts as the generalized force responsible for the relaxation process, while the former term is a generalized displacement. When the displacement term is small enough, it is possible to assume that the displacement and the force are linearly coupled, and thus the relaxation equation describing the rate at which any generic out-of-equilibrium state reaches the equilibrium one is given by

$$\frac{dU_e}{dt} = \alpha T_p^2\left(\frac{1}{T_p} - \frac{1}{T}\right), \tag{4}$$

where the proportionality coefficient α has the units W/K.

B. Phase-coexistence state

In a macroscopic system composed of many internal and interacting degrees of freedom, a first-order transition may occur differently than that described in the previous section. Indeed, the system may build up a mixture of the low- (LT) and high-temperature (HT) stable phases, separated by a phase boundary, because the phase coexistence may be more favorable from an energetic point of view. Specifically, the phase coexistence defines a transition temperature at equilibrium T_t which is obtained by means of the Maxwell construction. This construction consists of replacing the nonmonotonic part of $T_p(S)$, defined in Eq. (1), with the constant temperature T_t, as shown in Figs. 1 and 2. The latter is the temperature at which the two minima in the Gibbs-free-energy representation have the same value, i.e., $G_L(S_0;T_t) = G_L(S_1;T_t)$, where $G_L(S;T) = U_e(S) - TS$ and $S_0(T)$, $S_1(T)$ are the temperature-dependent minima of $G_L(S;T)$, satisfying $\partial G_L/\partial S|_{S=S_0} = \partial G_L/\partial S|_{S=S_1} = 0$. It is worth noting that S_0 and S_1 represent the entropies of the LT and HT stable magnetic phases which coexist at T_t. Specifically, from Eq. (1) and from the Maxwell construction, we obtain that the enthalpy-change rate at equilibrium and in the phase-coexistence region can be expressed as $dU_e/dt = T_t dS/dt$.

However, this equilibrium picture is not always realized. The nucleation and pinning of the phase boundary may occur at a sample temperature T that differs from T_t because of the local defects present in the material microstructure. This means that, when transforming in heating from the LT to the HT or, conversely, in cooling from the HT to the LT phase, a specific nucleation or pinning event i will be characterized by a critical value T_{hi} higher, or T_{ci} lower, than T_t (see Fig. 2). With T differing from the equilibrium value T_t, we consider also in this case the role of the entropy production processes introduced in Sec. II A. Analogous to Eq. (2), the entropy-change rate dS_i/dt associated with the ith event will be, in this case,

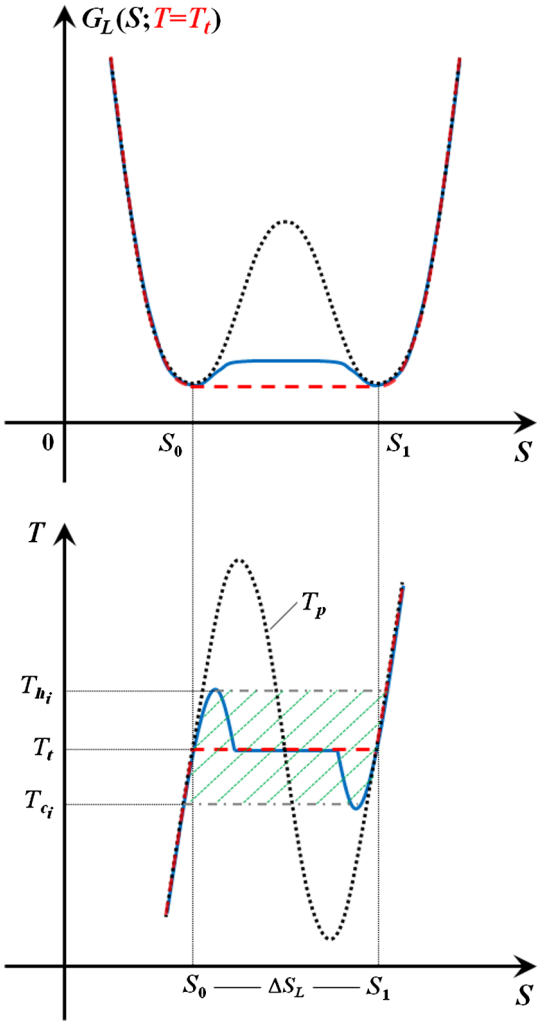

FIG. 2. (Top panel) Gibbs free energy $G_L(S;T=T_t)$ and (bottom panel) temperature $T=\partial U_e/\partial S$ vs entropy S, in first-order transitions, for (i) a homogeneous system (the black dotted line) in which the transition follows the T_p curve [Eq. (1)], (ii) a macroscopic system (the red dashed line) in which the transition occurs through the Maxwell construction at the equilibrium temperature T_t, and (iii) an irreversible domain nucleation event i (the pale-blue solid line) occurring around a defect at temperature T_{hi} (T_{ci}) upon heating (cooling). Green lines highlight the LT-HT phase-coexistence region. $\Delta S_L = S_1 - S_0$ is the entropy change at T_t between the entropies S_0, S_1 of the LT and HT stable magnetic phases.

$$\frac{dS_i}{dt} = \frac{1}{T}\frac{dU_{ei}}{dt} + \Sigma_{si}, \tag{5}$$

so that the entropy production rate will be given by

$$\Sigma_{si} = \left(\frac{1}{T_t} - \frac{1}{T}\right)\frac{dU_{ei}}{dt}. \tag{6}$$

In the latter equation, we recognize a velocity term, i.e., dU_{ei}/dt, and a displacement term, i.e., $1/T_t - 1/T$. By means of the same reasoning followed in Sec. II A to obtain Eq. (4), we end up with the following linear expression for the enthalpy-change rate occurring in the phase-coexistence region:

$$\frac{dU_{ei}}{dt} = \alpha_i T_t^2\left(\frac{1}{T_t} - \frac{1}{T}\right), \tag{7}$$

where the proportionality coefficient α_i associated with the microscopic event i again has the units W/K.

III. THERMAL TRANSPORT IN FIRST-ORDER PHASE TRANSITIONS

A. Constitutive kinetic equation for the material

The thermal transport in a macroscopic solid-state system is described by its constitutive equation that locally takes the form of a continuity equation for the energy [64,68,69]:

$$c_s\frac{\partial T}{\partial t} + \boldsymbol{\nabla}\cdot\boldsymbol{j}_q = -\frac{\partial u_e}{\partial t}. \tag{8}$$

The first term on the left-hand side of Eq. (8) describes the specific heat c_s of the system arising from the electronic and structural reversible contributions. The second term on the left-hand side takes into account the heat current density $\boldsymbol{j}_q$ flowing through the sample. Finally, the term on the right-hand side of Eq. (8) describes a source or sink for the heat flux that, in a first-order magnetic transition, is represented by the specific latent heat $\partial u_e/\partial t$ absorbed or released by the system.

It is now convenient to introduce the typical linear size λ, over which the temperature T is uniform into the sample (see Fig. 3 for a schematic view of the typical length scales involved in the description of the irreversible events occurring in a first-order magnetic phase transition). By performing the integration of the continuity equation (8) over the volume λ^3, we get the following relation describing the latent heat of the system:

$$\frac{dU_e}{dt} = -\left(C_s\frac{dT}{dt} + \int_{\lambda^2}\boldsymbol{j}_q\cdot\boldsymbol{n}d^2r\right). \tag{9}$$

In Eq. (9), $U_e = \lambda^3 u_e$ and $C_s = \lambda^3 c_s$ are the enthalpy and heat capacity of the region of the sample involved in the phase transformation, respectively, and the last term at the right-hand side is obtained by means of the divergence theorem, with $\boldsymbol{n}$ being the outward-pointing unit vector orthogonal to the surface and λ^2 being the surface area encompassing the integration volume.

We can get another expression for the latent heat dU_e/dt by relating the latter to the microscopic events i giving rise to the phase transition. We will assume that the transition is driven by the motion of the phase-boundary interface separating the LT and HT magnetic states, which is

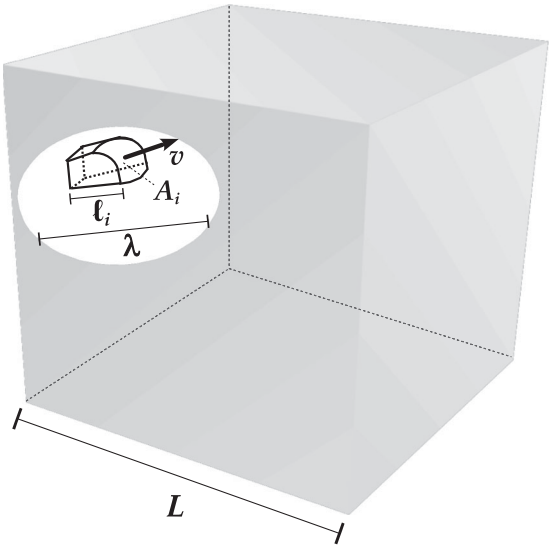

FIG. 3. Typical length scales involved in the irreversible events driving a MCE system through a first-order magnetic transition. L is the linear size of the sample, λ represents the linear size of the region in which T is uniform, and ℓ_i is the linear size of the region swept out by the ith piece of boundary interface of surface area $A_i \sim \ell_i^2$ during its motion at velocity v [see Eq. (12)]. The size λ depends on the heat-diffusion properties of the system and can be either $\ll L$ for macroscopic samples or $\gtrsim L$ for small fragments; the size ℓ_i depends instead on the material microstructure and, in this work, we assume $\ell_i \ll \lambda$.

nucleated at the defects present in the material microstructure, as explained in Sec. II B. This interface can be thought of as a surface of total area A that moves with a certain velocity and is composed by several portions characterized by surface area A_i, so that $A = \sum_i A_i$. If we assume to deal with an ideally thin interface, the phase transformation will be due to the displacement of the position of the interface in time, $x(t)$, and the latent heat can be expressed as

$$\frac{dU_e}{dt} = \Delta u_L A \frac{dx}{dt}, \tag{10}$$

where $\Delta u_L = T_t \Delta s_L > 0$ is the enthalpy change per unit volume at T_t (see Fig. 1) and Δs_L is the isothermal entropy density change at the transition. Specifically, from Eq. (10), we can obtain the enthalpy-change rate associated with the motion of any individual portion A_i of the boundary interface, given by

$$\frac{dU_{ei}}{dt} = \Delta u_L A_i \frac{dx}{dt}. \tag{11}$$

On the one hand, by substituting Eq. (11) into Eq. (7) and by defining the proportionality coefficient $\alpha_s = \alpha_i / A_i$, having units $\mathrm{W\,K^{-1}\,m^{-2}}$, we immediately get the following expression for the velocity of the phase-boundary interface:

$$\frac{dx}{dt} = \frac{\alpha_s}{\Delta u_L} T_t^2 \left(\frac{1}{T_t} - \frac{1}{T} \right). \tag{12}$$

It is worth noting that Eq. (12), through the coefficient α_s, encompasses the details of the damping mechanisms of the phase-boundary motion, thus describing the kinetics of the relaxation processes occurring at first-order phase transitions in macroscopic systems. On the other hand, by substituting Eq. (12) back into Eq. (10) and assuming that $T \simeq T_t$, we obtain the expression for the latent heat of the system:

$$\frac{dU_e}{dt} \simeq \alpha_s A (T - T_t) = \sum_i \alpha_s A_i (T - T_t). \tag{13}$$

Finally, the comparison of Eq. (9) to Eq. (13) allows us to determine the following expression for the heat current flux:

$$\frac{1}{\lambda^3} \int_{\lambda^2} \boldsymbol{j}_q \cdot \boldsymbol{n} d^2 r = -c_s \frac{dT}{dt} - \sum_i \alpha_s \frac{A_i}{\lambda^3} (T - T_t). \tag{14}$$

It is worth pointing out that each of the microscopic events i contributing to the sum in Eq. (14) is activated at its own temperature $T_{hi} > T_t$ in a heating process, or $T_{ci} < T_t$ in the cooling case, as described in Sec. II B and depicted in Fig. 2. This fact indicates that the motion of each portion of the boundary surface is activated by overcoming different energy barriers. Then, Eq. (14) shows that the events i within the volume λ^3 are correlated because the activation of a certain single event will cause the decrease—upon heating—or the increase—upon cooling—of the temperature T within the whole volume λ^3, therefore inhibiting the activation of the other domains' motion.

B. Kinetics in quasi-isothermal conditions

In order to unveil the local variations of the sample temperature T occurring in a phase transition caused by the presence of a distribution of different activation temperatures T_{ci}, T_{hi}, let us consider connecting the MCE sample to a thermal reservoir having uniform temperature T_b, through a thermal contact. The latter is conveniently represented as a region characterized by a surface area A_c and a thickness t_c. The current density $j_q = \|\boldsymbol{j}_q\|$ associated with the heat flowing through the contact along the direction orthogonal to the surface A_c is then given by

$$j_q = -\kappa_c \frac{T_b - T}{t_c}, \tag{15}$$

where κ_c is the thermal conductivity of the contact and, in the equality, we assume that the temperature varies linearly inside the contact thickness t_c.

The current density $\boldsymbol{j}_q$ is also related to the specific and latent heat through Eq. (14). In what follows, we will limit

ourselves to investigating the case in which the temperature T can be considered uniform in the whole sample, so that we can neglect the role of the heat-diffusion processes occurring inside the sample itself. This assumption is valid when the macroscopic linear size of the sample L (see Fig. 3) is smaller than λ and the thermal conductivity κ of the MCE material, appearing in the relation $\boldsymbol{j}_q = -\kappa \boldsymbol{\nabla} T$, is high. With the above assumptions, we can immediately evaluate the heat current flowing through the sample surface by substituting Eq. (15) into the left-hand side of Eq. (14), and, in this way, we obtain the differential equation governing the time behavior of $T(t)$ during the phase transition:

$$\frac{dT}{dt} = \frac{\kappa_c}{\lambda c_s t_c}(T_b - T) - \sum_i \frac{\alpha_s A_i}{\lambda^3 c_s}(T - T_t) = \frac{T_b - T}{\tau_c} - \sum_i \frac{T - T_t}{\tau_{si}}. \quad (16)$$

In Eq. (16), we define the time constants $\tau_c = \lambda c_s t_c/\kappa_c$ and $\tau_{si} = \lambda^3 c_s/(\alpha_s A_i)$. While the latter, through the coefficient α_s and the typical sizes λ and A_i, is related only to the intrinsic kinetics and the damping mechanisms governing the phase transition, the former takes into account the role of the external thermal reservoir through the thermal contact resistance $t_c/(\kappa_c A_c)$.

The solution of Eq. (16) is strictly dependent not only on the initial conditions on T but also on the time behavior of the thermal reservoir temperature $T_b(t)$. There are two cases of particular interest: (i) a constant T_b and (ii) T_b varying at a constant rate $\dot{T}_b$. The former condition ensures that the motion of each piece of boundary interface of surface area A_i is separated in time from the other ones. This circumstance happens because when the surface A_i starts to move, the temperature T becomes lower than T_{hi} upon heating, or higher than T_{ci} upon cooling, in a volume λ^3 which, in our case, corresponds to the whole sample since we are assuming $L < \lambda$, in this way inhibiting the occurrence of other events. This case is described in detail in Sec. III C and Appendix A.

The case of a reservoir temperature T_b varying in time at a constant rate $\dot{T}_b$ is also very interesting from both a physical and a mathematical point of view. Indeed, when T_b varies uniformly in time, many events i, with each corresponding to the motion of a piece of boundary surface A_i, may occur concurrently and may collectively contribute to the sum appearing on the right-hand side of Eq. (16). This fact happens because the heat provided by the thermal bath to the MCE sample during the phase transition is enough to overcome the change in temperature occurring within the λ^3 volume. The solution $T(t)$ shows, in this case, many qualitatively interesting features, and it is derived in Appendix B.

C. Kinetics of individual avalanches

Let us address now the case of a thermal reservoir temperature T_b kept constant in time during the phase transition. Then, as explained in Sec. III B, we can further simplify Eq. (16) because, in this case, the individual events i associated with the motion of the portions of boundary interface of surface area A_i, are well separated in time. For the sake of simplicity, we assume from here on that $A_i \sim \ell_i^2$, meaning that the surface area of each portion of the boundary interface scales as the square of the typical linear size ℓ_i covered by the interface during its motion (see Fig. 3). It is worth noting that the ℓ_i value is strictly related to the sample microstructure determining the nucleation and pinning centers for the formation of a new phase, and we will assume $\ell_i \ll \lambda$. In this way, we can consider these events as independent of each other, and we can investigate the effect that each of them, taken one at a time, has on the time evolution of T. This assumption means that the sum appearing in Eq. (16) reduces to only one term and, therefore, by defining t_i, t_f as the times at which the event starts and ends, we can conclude that the time behavior of T during a first-order transition driven by a single irreversible event is governed by the following differential equation:

$$\frac{dT}{dt} = \frac{T_b - T}{\tau_c} - \frac{T - T_t}{\tau_{si}}, \quad \text{for } t_i \le t \le t_f. \quad (17)$$

For $t > t_f$, once the transition ends, the contribution of the latent heat associated with the boundary motion is no longer present in Eq. (14), and the differential equation governing the behavior of the sample temperature $T(t)$ is

$$\frac{dT}{dt} = \frac{T_b - T}{\tau_c}, \quad \text{for } t > t_f. \quad (18)$$

It is worth noting that Eq. (17) describes the system during the phase transition, when T varies because of both the effect of the external thermal contacts and of the intrinsic kinetics of the moving boundary interface which absorbs or releases heat, depending on whether we are dealing with a heating or cooling process, thus reducing or enhancing T with respect to its initial value. On the other hand, Eq. (18) describes the behavior of the system once the transition ends and the temperature T relaxes back to the thermodynamic equilibrium value governed only by the heat exchanged with the thermal reservoir.

The solutions of Eqs. (17) and (18) for a constant T_b and $t_f - t_i \ll \tau_c, \tau_{si}$ are analytically derived in Appendix A. It is worth pointing out that the condition $t_f - t_i \ll \tau_c, \tau_{si}$ ensures that the sample temperature T—and, consequently, the heat flux $q_s(t)$—is far from the thermodynamic equilibrium during the whole phase transition and that the transformation thus occurs through a sequence of out-of-equilibrium states far from T_t (see also Fig. 2). Specifically, the time behavior of the heat flux $q_{si}(t)$ for an individual avalanche is given by

$$q_{si}(t) = \begin{cases} \pm\frac{\lambda^3 c_s}{\tau_c \tau_{si}} \frac{\Delta T^{\rm hyst}}{2}(t - t_i), & \text{for } t_i \le t \le t_f, \\ \pm|q_{si}(t_f)| e^{-[(t-t_f)/\tau_c]}, & \text{for } t > t_f, \end{cases} \quad (19)$$

where the plus sign holds in a heating process so that $q_{si}(t) > 0$, the minus sign holds for the cooling case so that $q_{si}(t) < 0$, $|q_{si}(t_f)| = \lambda^3 c_s \Delta T^{\rm hyst}(t_f - t_i)/(2\tau_c\tau_{si})$ is the heat flux at the end of the phase transition when $t = t_f$ and $\Delta T^{\rm hyst} = T_{hi} - T_{ci} > 0$ is the temperature hysteresis between the heating, i.e., T_{hi}, and the cooling, i.e., T_{ci}, transition temperatures of each avalanche. For the sake of simplicity, in what follows, we assume $\Delta T^{\rm hyst}$ to be the same for all of the avalanches detected at a given field H, meaning that the temperature hysteresis depends only on H, not on the single microscopic irreversible events i driving the transition. Moreover, we will choose T_{hi} and T_{ci} to be symmetric around T_t (see Fig. 2). In this way, $T_t = (T_{hi} + T_{ci})/2$ and $\Delta T^{\rm hyst}/2 = T_{hi} - T_t = T_t - T_{ci}$.

It is important to point out that, in the case of slow scan rates and far-from-equilibrium avalanches that we are considering, the theoretically expected behavior of the heat-flux signal during the transition, i.e., for $t_i \le t \le t_f$, is linear in time and governed by both of the time constants τ_{si} and τ_c, while the subsequent relaxation towards the equilibrium is described by an exponential law governed by the time constant τ_c alone, related to the thermal contact details only.

IV. COMPARISON WITH EXPERIMENTS

We analyze the experimental data obtained by performing Peltier calorimetry temperature scans at different rates and at various applied magnetic fields H on a series of $La(Fe\text{-}Mn\text{-}Si)_{13}\text{-}H_{1.65}$ samples. Indeed, these kinds of experiments, in which a calorimeter evaluates the heat flux exchanged between the sample and the external thermostat by performing temperature or magnetic-field scans at different rates [70,71], are the right ones to apply the theoretical model developed in Sec. III. The sample preparation and the experimental procedure followed to detect the heat-flux signals are detailed in Ref. [54]. Specifically, in Ref. [54], it was shown that the heat-flux signals present well-separated avalanches only when the temperature scans are performed at very low rates, i.e., lower than 20 mK/s, on small fragments of the material under investigation characterized by a mass of a few milligrams. We focus our analysis on the data obtained through scans performed in heating at the lowest scan rate, i.e., $dT_b/dt = 1$ mK/s, on two samples of the series characterized by nominal compositions Mn = 0.18 and Mn = 0.30. The mass of the samples is $m_1 = 4.79$ mg and $m_2 = 5.26$ mg for the two compositions 0.18 and 0.30, respectively. It is worth noting that such small masses allow us to assume from here on that $\lambda = L$, meaning that the sample temperature T will be considered uniform within the whole sample.

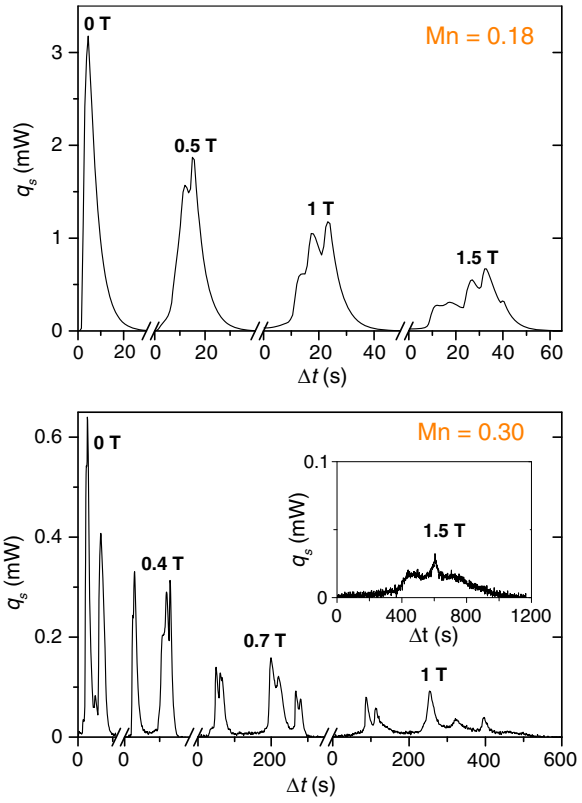

FIG. 4. Heat flux q_s as a function of time at different magnetic fields $\mu_0 H$. Experimental data obtained by Peltier calorimetry temperature scans performed at a rate of $dT_b/dt = 1$ mK/s, upon heating, on the (top panel) $LaFe_{11.60}Mn_{0.18}Si_{1.22}\text{-}H_{1.65}$ and (bottom panel) $LaFe_{11.41}Mn_{0.30}Si_{1.29}\text{-}H_{1.65}$ samples.

The resulting heat-flux signals as a function of time for different fields H varying between 0 and 1.5 T and around the transition temperature T_t are reported in Fig. 4. The data clearly show the presence of avalanches separated in time in both samples, increasing in number and changing in shape by approaching the critical field H_c of the system, at which the phase transition becomes second order, given by $H_c \simeq 2.3$ T and $H_c \simeq 1.2$ T for Mn = 0.18 and Mn = 0.30, respectively [72]. All of the avalanches are characterized by a fast linear growth followed by a longer exponential decay. To interpret this kind of behavior theoretically, we can notice that since the experimental temperature scans are performed at a very low rate for each field H, we can safely treat the thermostat temperature T_b as a constant during the phase transition. Then, we describe the time behavior of the avalanches using Eq. (19) of Sec. III C.

First, we obtain the values of τ_c by performing the fit of the exponential decays observed in selected avalanches of both samples at various H values, as shown in Fig. 5. The resulting average values $\langle\tau_c\rangle$ for the various H and Mn compositions are reported in Table I. We then fit the linear rises with the function $q_{si}(t) = a(t - t_i)$. From the first equation in Eq. (19), the slope a can be written as

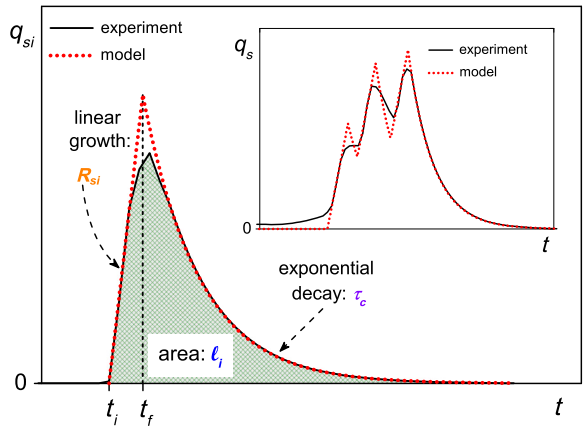

FIG. 5. Example of the fit of an individual avalanche: fitting curves to Eq. (19) (the red dotted line) and the experimental data (the black solid line). The fit of linear rise, exponential decay, and area under the curve allow us to determine the parameters R_{si}, τ_c, and ℓ_i, respectively. (Inset) Example of the fit in the case of a multiple avalanche.

$a = (R_{si}/\tau_c)\Delta T^{\text{hyst}}/2$, where we define the quantity $R_{si} = (\alpha_s A_i)^{-1} = (\alpha_s \ell_i^2)^{-1}$, having the units of a thermal resistance, i.e., K/W. Specifically, from the definition of R_{si}, we notice that it accounts only for the internal damping mechanism driving the system through the phase transition, not for the contact details. The choice of evaluating R_{si} instead of τ_{si} lies on the difficulty of estimating the reversible contribution to the specific heat of the system c_s close to the transition temperature T_t. By using the values of τ_c and those of the temperature hysteresis $\Delta T^{\text{hyst}}/2$ experimentally determined [54,72] and reported in Table I and Fig. 7, it is possible to evaluate R_{si}. The behavior of R_{si} for the avalanches analyzed is reported in Fig. 6(a).

In order to evaluate the damping coefficient α_s, we need to evaluate the linear size ℓ_i associated with each resistance value R_{si}. ℓ_i is obtained by computing the latent heat exchanged in each region of the sample involved in the phase transition with the surroundings. As shown in Sec. II B, the latent heat is related to the volume $\ell_i A_i \sim \ell_i^3$ covered by the boundary interface during its motion through Eq. (10), so $\ell_i = \{[\int q_{si}(t)dt]/\Delta u_L\}^{1/3}$. Thus, by integrating the individual heat-flux avalanches detected experimentally (see Fig. 4) between the times corresponding to the beginning of the avalanche and those

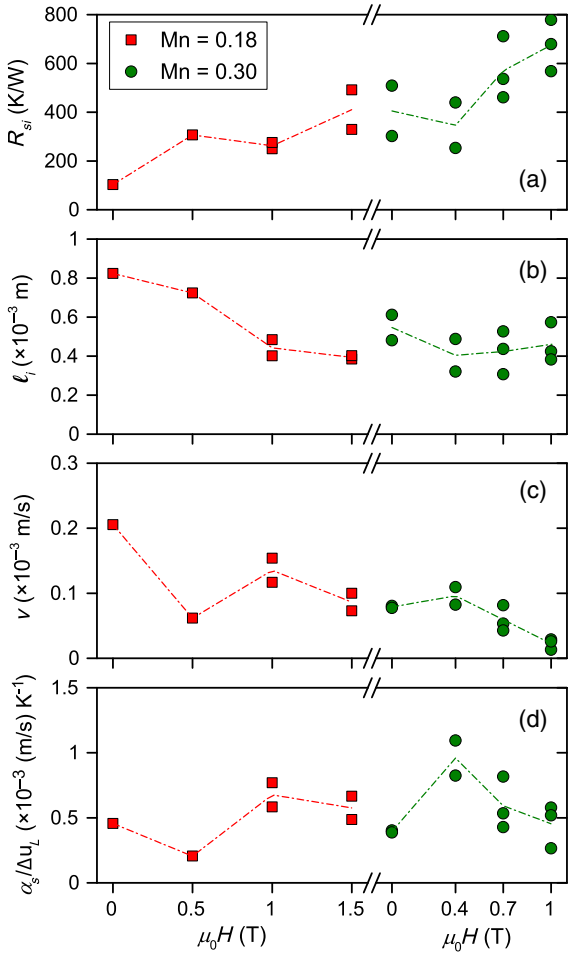

FIG. 6. (a) Damping resistance R_{si}, (b) linear size ℓ_i, (c) velocity $v = dx/dt$, and (d) ratio $\alpha_s/\Delta u_L$, as a function of the applied field $\mu_0 H$, for La(Fe-Mn-Si)$_{13}$-H samples with nominal compositions Mn = 0.18 (the red squares) and Mn = 0.30 (the green circles). Points are obtained by fitting the avalanches shown in Fig. 4 through Eq. (19) with the parameters reported in Table I. The dashed-dotted lines connecting the average values among points serve as a guide for the eye.

TABLE I. Experimental values of T_t, $\Delta T^{\text{hyst}}/2$, and $\Delta u_L = T_t \Delta s_L$, obtained by Peltier calorimetry temperature scans at different magnetic fields $\mu_0 H$ on La(Fe-Mn-Si)$_{13}$-H samples with Mn = 0.18 and Mn = 0.30 (density $\rho = 7200$ kg/m^3), following Refs. [54,72]. The average values $\langle \tau_c \rangle$ are evaluated by fitting the decay parts of the heat-flux avalanches (Fig. 4) with the exponential law of Eq. (19), as depicted in Fig. 5.

Mn = 0.18					Mn = 0.30				
$\mu_0 H$ (T)	T_t (K)	$\Delta T^{\text{hyst}}/2$ (K)	Δu_L (×10^6 J/m^3)	$\langle \tau_c \rangle$ (s)	$\mu_0 H$ (T)	T_t (K)	$\Delta T^{\text{hyst}}/2$ (K)	Δu_L (×10^6 J/m^3)	$\langle \tau_c \rangle$ (s)
0	321.4	0.45	31.2	4.0	0	295.8	0.2	21.9	6.1
0.5	323.1	0.3	30.2	4.1	0.4	297.6	0.1	20.1	5.8
1	325.1	0.2	29.3	4.2	0.7	298.6	0.1	18.3	10.5
1.5	326.7	0.15	28.2	4.6	1	300.5	0.05	16.9	22.0

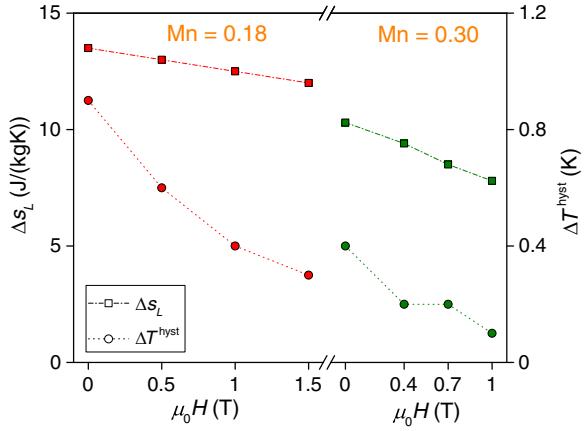

FIG. 7. Experimental values of entropy change per unit mass Δs_L at T_t (the squares; scale on the left axis) and of temperature hysteresis ΔT^{hyst} (the circles; scale on the right axis), as a function of the applied field $\mu_0 H$, for La(Fe-Mn-Si)$_{13}$-H compounds with nominal compositions Mn = 0.18 (the red symbols) and Mn = 0.30 (the green symbols).

corresponding to the end of its exponential decay (see Fig. 5), and by using the experimental values for $\Delta u_L = T_t \Delta s_L$ reported in Table I (see also Fig. 7), we find the ℓ_i values reported in Fig. 6(b).

Finally, we evaluate the damping coefficient α_s through the internal resistance R_{si} and the size ℓ_i as $\alpha_s = 1/(R_{si}\ell_i^2)$. In this way, we can also estimate the starting velocity of the boundary interface $v = dx/dt = (\alpha_s/\Delta u_L)\Delta T^{hyst}/2$, a relation obtained by approximating Eq. (12) for $T \simeq T_t$. The behavior of v, together with the values of the ratio $\alpha_s/\Delta u_L$, are shown in Figs. 6(c) and 6(d) for various magnetic fields H and different Mn compositions.

V. DISCUSSION

As a first result of the fitting of the experimental avalanches with the model, we can observe that R_{si}, beyond depending on the Mn composition, increases by increasing the applied magnetic field H [Fig. 6(a)]. The opposite behavior characterizes the typical size ℓ_i swept out by each piece of the domain boundary interface during its motion [Fig. 6(b)]. Such a decrease in ℓ_i, and hence in the volume ℓ_i^3 of each individual avalanche, is consistent with the increase in the number of avalanches which are experimentally detected when approaching the critical point of the system (see Fig. 4) since the volume that transforms during the transition from a certain phase to a new one is $\lambda^3 \sim \sum_i \ell_i^3$.

This kind of behavior is not trivial, and it may be interpreted as a consequence of the assumption that the transition is driven by the heterogeneous nucleation and pinning of the boundaries of the new phase at the defects present in the MCE sample. The applied field H can be thought of as acting on the typical energy profile characterizing a first-order transition (Fig. 2) by modulating the energy barrier between the stable phases S_0 and S_1—and hence decreasing the temperature hysteresis ΔT^{hyst}—as shown in the bottom of Fig. 7, without affecting the material microstructure. In this way, it is possible to distinguish three different regimes depending upon the values of the applied field H. When H is far below the critical point and, eventually, $H \sim 0$, the energy barrier and the hysteresis are high enough to prevent many defects of the sample to be active as nucleation centers of the new phase. As a consequence, when the new phase nucleates at a certain point, the subsequent transformation involves the whole sample and a single avalanche is observed. At higher H but still below H_c, the energy barrier and ΔT^{hyst} are reduced and the nucleation and growth of new domains may occur in several points of the sample. Then, more avalanches, still well separated in time, come into play and are experimentally detected. Finally, by further increasing H and getting closer to H_c—or even above it—the hysteresis reduces essentially to zero and a proliferation of avalanches superimposing each other is observed. The number of avalanches is so high that they are blurred in an almost continuous background, and the single peaks cannot be distinguished anymore.

The situation described here can be efficiently illustrated by choosing several samples having different critical points H_c, so that a given applied field H may be well below H_c, at an intermediate level between 0 and H_c, or close to or higher than H_c, depending upon the specific sample under investigation. This situation is well represented by the compounds of the La(Fe-Mn-Si)$_{13}$-H$_{1.65}$ series that we consider here. Indeed, an applied field $H \sim 1.5$ T is already higher than $H_c \sim 1.2$ T for the Mn = 0.30 sample, but it is still below $H_c \sim 2.3$ T in the case Mn = 0.18. This circumstance is well reflected in the behavior of the heat-flux signals detected at this field on the two compounds. These signals indeed show a pattern already demonstrated in separated avalanches for Mn = 0.18 and, on the contrary, a rather continuous background for Mn = 0.30 (see Fig. 4 and the inset therein).

Interestingly, the increase in R_{si} and the decrease in ℓ_i observed by increasing H compensate for each other, so that the parameter $\alpha_s/\Delta u_L = (R_{si}\ell_i^2 \Delta u_L)^{-1}$ appearing in Eq. (12) is essentially constant, independent of H and of the material composition [Fig. 6(d)]. The average value of this parameter, representing the starting velocity of the moving phase-boundary interface corresponding to a variation in temperature of 1 K, amounts to $\alpha_s/\Delta u_L \approx 0.5 \times 10^{-3}\,(\mathrm{m/s})\,\mathrm{K}^{-1}$.

Another important feature to mention is that the velocity $v = dx/dt$ of the heat-flux avalanches shows a clear decrease by enhancing H and getting closer to H_c [Fig. 6(c)], meaning that the associated boundary motion slows down by approaching the critical point of the system.

This kind of behavior may be interpreted as a manifestation of the critical slowing down known to appear around the critical point of a phase transition [73,74], and it can be ascribed to the disappearance of the avalanches above H_c.

A final comment concerns the role played by the intrinsic kinetics governing the transition, with respect to extrinsic factors, in affecting the heat exchanged between the MCE sample and its surroundings. A comparison between the R_{si} values and the contact resistance values R_c can be made. A rough estimate of R_c can be obtained from the average values $\langle\tau_c\rangle$ reported in Table I for different fields H and for different nominal Mn compositions. In order to relate R_c to $\langle\tau_c\rangle$, we must take into account the fact that, for the particular measuring setup we have employed to perform the temperature scans, the thermal contacts also comprise the Peltier cells of the calorimeter which are characterized by their own resistance and capacity, R_P and C_P, respectively. Both of these quantities can be determined by calibrating the calorimeter, and they evaluate to $R_P = 75$ K/W and $C_P = 48$ mJ/K [71]. Then, by also including the contribution associated with C_P, the thermal contact resistance can be expressed as $R_c = \langle\tau_c\rangle/(C_s + C_P)$. The heat capacity $C_s = \lambda^3 c_s$ may be evaluated by observing that λ^3 represents, in our case, the whole sample volume since we have assumed $\lambda = L$, and the specific heat c_s around the transition temperature at various H values can be extrapolated from the experimental data reported in Ref. [72]. With $c_s \simeq 600$ J/(kg K) for Mn = 0.18, essentially not dependent on H, and $c_s \simeq 1000$ J/(kg K) at $H = 0$ T and $c_s \simeq 1500$ J/(kg K) at $H = 1$ T for Mn = 0.30, we can conclude that $R_c \sim 80$–90 K/W in the Mn = 0.18 case, while $R_c \sim 100$–400 K/W for Mn = 0.30. We can notice that the R_c and R_{si} values have the same order of magnitude for both of the compositions considered here. We can conclude that it would be attractive to envisage the development of experiments able to enhance R_c with respect to R_{si}, or vice versa, by choosing the right MCE materials and measuring setup. In this way, it would be possible to clearly distinguish the effects on the heat-flux exchange due to the intrinsic kinetics and to extrinsic factors, such as the measurement system. Such an investigation will be the subject of future work.

VI. CONCLUSIONS

In this paper, we introduce a thermodynamic model describing the out-of-equilibrium effects proper in first-order phase transitions to analyze the heat-flux signals experimentally observed by performing temperature scans at low rate on a series of $La(Fe\text{-}Mn\text{-}Si)_{13}\text{-}H_{1.65}$ fragments with Mn = 0.18 and Mn = 0.30. The physical picture arising from the comparison between the experimental data and the model is coherent with the assumption of a defect-driven phase transition, in which the system transforms from a magnetically ordered LT-FM phase to a disordered HT-PM phase because of the motion of the domain boundaries which nucleate at the defects present in the material microstructure.

Specifically, we show that, when the scan rate is low enough, the nucleation and pinning centers of the sample are active one at a time, and they give rise to characteristic repeatable series of heat-flux peaks which have a typical linear growth followed by an exponential decay. We relate the appearance of these avalanches to individual, well-time-separated, independent boundary motion events associated with the latent heat of the system. Furthermore, we show that the nontrivial patterns experimentally observed in the heat-flux signals can be interpreted as a consequence of the applied magnetic field H. The latter modulates the energy profile and the hysteresis of the system by getting closer to the critical point H_c, and it affects in this way the number of nucleation centers that may be active in the sample.

Finally, we evaluate the coefficient α_s associated with the internal damping of the boundary motion events for the $La(Fe\text{-}Mn\text{-}Si)_{13}\text{-}H_{1.65}$ compounds. Although a precise quantitative estimate of this parameter is limited by the limited amount of available experimental data, we find a value α_s which is essentially not dependent on either the applied magnetic field H or the Mn composition. This outcome suggests that α_s may be considered as a parameter related only to the intrinsic properties of each class of MCE materials.

APPENDIX A: CONSTANT T_b

The case of a constant thermal reservoir temperature T_b allows us to properly describe calorimetry measurements in which the temperature scans are performed at very low rates. In this regime, the single avalanches observed in the heat-flux signal are well separated in time and are distinguishable from a uniform background, so it is possible to follow the time evolution of each of them. The appearance of each avalanche is due to individual nucleation and pinning events occurring in many different regions of the sample which are active at different subsequent times. The separation in time of these events can be explained by supposing that when the transition begins, the phase-boundary interface will start to move around a certain nucleation center, exchanging heat and causing the variation of the sample temperature T within a typical volume λ^3 (see Fig. 3) around the nucleation center. This change in temperature will prevent the occurrence of other nucleation events and boundary motions inside the same volume since T will be different from the threshold value necessary for the motion of the boundary interface, i.e., T_{hi} in a heating process or T_{ci} in the cooling case (see Sec. II B). Once the phase boundary will stop and the heat-flux avalanche will end, the whole region will relax again towards the equilibrium temperature T_{hi} or T_{ci}, thus allowing a new avalanche to start. The presence of an applied magnetic

field H does not affect this picture, even if H is close to the critical value H_c. Indeed, the increase in the H value is reflected in a decrease of the temperature hysteresis $\Delta T^{\rm hyst}$ and in the consequent increase of the number of the active regions of the sample in which an avalanche event may occur. Therefore, by increasing H the number of individual avalanches experimentally detected is also increased. However, the separation in time among these avalanches depends on the heat exchanged by the boundary interface with the surrounding region of the sample and with the external thermal reservoir and this feature is related only to the internal properties of the material and to the external scan rate, but it cannot be affected by H.

The differential equations governing the time behavior of the sample temperature $T(t)$ are derived in Sec. III and are given by Eqs. (17) and (18). To solve these equations, we assume that the transition starts at $T(t_i) = T_{hi}$ for a heating process [$T(t_i) = T_{ci}$ for the cooling case]. Then the constant T_b value is $T_b = T_{hi}$ in heating ($T_b = T_{ci}$ in cooling). The solution of Eqs. (17) and (18) for an individual avalanche is then

$$T(t) = \begin{cases} T(t_i) \mp \frac{\tau_c}{\tau_c+\tau_{si}} \frac{\Delta T^{\rm hyst}}{2} (1 - e^{-[(t-t_i)/\tau_{sc}]}), & \text{for } t_i \le t \le t_f, \\ T(t_i) \mp |T(t_i) - T(t_f)| e^{-[(t-t_f)/\tau_c]}, & \text{for } t > t_f, \end{cases} \tag{A1}$$

where $T(t_i) = T_{hi}$ and the minus sign hold for a heating process, while $T(t_i) = T_{ci}$ and the plus sign hold in the cooling case, and we introduce the quantity $|T(t_i) - T(t_f)| = \tau_c/(\tau_c+\tau_{si})(\Delta T^{\rm hyst}/2)(1-e^{-[(t_f-t_i)/\tau_{sc}]}) > 0$, with $\Delta T^{\rm hyst} = T_{hi} - T_{ci}$ and $\Delta T^{\rm hyst}/2 = T_{hi} - T_t = T_t - T_{ci}$. Moreover, in Eq. (A1), we define the time constant $\tau_{sc} = (1/\tau_c + 1/\tau_{si})^{-1} = \lambda^3 c_s (\lambda^2 \kappa_c/t_c + \alpha_s \ell_i^2)^{-1}$. We observe that the time constant τ_{sc}, governing the behavior of T during the transition, is the parallel of the time constants τ_c, τ_{si} defined in Sec. III C, and therefore it is dominated by the smaller one between them. This observation implies that the heat exchanged between the boundary interface and the surrounding region of the sample during the phase transition can be governed either by the intrinsic damping ($\tau_{si} \ll \tau_c$) or by external factors only ($\tau_{si} \gg \tau_c$). Specifically, since we are assuming that $\ell_i \ll \lambda$ (see Sec. III C and Fig. 3) and that the contact resistance $t_c/(\kappa_c A_c)$ for the samples investigated here is low (see Ref. [54]), the internal time constant τ_{si} is expected to be higher than the τ_c for any event i, so that $\tau_{sc} \simeq \tau_c$. In this respect, it is worth noting that, from an analytical point of view, the time constants τ_{si} and τ_c can be independently determined and do not mix together if the individual heat-flux avalanches associated with the transition event are far from equilibrium during the whole transition, a condition which is realized if $t_f - t_i \ll \tau_{sc}$. Indeed, in this case, we have $\exp[-(t-t_i)/\tau_{sc}] \simeq 1 - (t-t_i)/\tau_{sc}$, and the first row of Eq. (A1) assumes the form $T(t) - T(t_i) \simeq \mp (\Delta T^{\rm hyst}/2)(t-t_i)/\tau_{si}$ independent of whether $\tau_{si} \ll \tau_c$ or $\tau_{si} \gg \tau_c$. Then, we can conclude that in the case of far-from-equilibrium avalanches, the sample temperature T will vary linearly in time with a slope determined only by the internal time constant τ_{si} for $t_i \le t \le t_f$, while it will relax back to the equilibrium for $t > t_f$, with an exponential law governed only by the time constant τ_c.

The solution given by Eq. (A1), combined with Eq. (15), allows us to determine the time behavior of the heat current density $j_q(t)$ flowing through the thermal contact for an individual avalanche event, which reads

$$j_q(t) = \begin{cases} \mp \frac{\lambda c_s}{\tau_c+\tau_{si}} \frac{\Delta T^{\rm hyst}}{2} (1 - e^{-[(t-t_i)/\tau_{sc}]}), & \text{for } t_i \le t \le t_f, \\ \mp |j_q(t_f)| e^{-[(t-t_f)/\tau_c]}, & \text{for } t > t_f, \end{cases} \tag{A2}$$

with $|j_q(t_f)| = \lambda c_s |T(t_i) - T(t_f)|/\tau_c$ being the modulus of the heat current density at $t = t_f$, the minus sign holding for a heating process, and the plus sign holding for the cooling case.

Finally, from Eq. (A2) and by integrating the continuity equation (8) on the volume λ^3 enclosed in the surface area λ^2, we obtain the time behavior of an individual heat-flux avalanche $q_{si}(t) = -\lambda^2 j_q(t)$:

$$q_{si}(t) = \begin{cases} \pm \frac{\lambda^3 c_s}{\tau_c+\tau_{si}} \frac{\Delta T^{\rm hyst}}{2} (1 - e^{-[(t-t_i)/\tau_{sc}]}), & \text{for } t_i \le t \le t_f, \\ \pm |q_{si}(t_f)| e^{-[(t-t_f)/\tau_c]}, & \text{for } t > t_f, \end{cases} \tag{A3}$$

where, in this case, $|q_{si}(t_f)| = \lambda^3 c_s |T(t_i) - T(t_f)|/\tau_c$ is the modulus of the heat flux at $t = t_f$, the plus sign holds for heating so that $q_{si}(t) > 0$, and the minus sign holds for cooling so that $q_{si}(t) < 0$. Again, if the avalanches are far from equilibrium, and hence $t_f - t_i \ll \tau_{sc}$, the heat-flux behavior during the transition becomes linear in time and is governed by both of the time constants τ_{si} and τ_c, while the subsequent relaxation towards equilibrium can still be described by an exponential law governed by the time constant τ_c related to the thermal contact details only:

$$q_{si}(t) = \begin{cases} \pm \frac{\lambda^3 c_s}{\tau_c \tau_{si}} \frac{\Delta T^{\rm hyst}}{2} (t - t_i), & \text{for } t_i \le t \le t_f, \\ \pm |q_{si}(t_f)| e^{-[(t-t_f)/\tau_c]}, & \text{for } t > t_f, \end{cases} \tag{A4}$$

with $|q_{si}(t_f)| = \lambda^3 c_s \Delta T^{\rm hyst} (t_f - t_i)/(2\tau_c \tau_{si})$.

APPENDIX B: T_b VARYING AT CONSTANT RATE $\dot{T}_b$

The case of a thermal reservoir temperature T_b varying at a constant rate $\dot{T}_b$ applies to the description of

calorimetry experiments performed at high scan rates. Contrary to the case discussed in Appendix A, the high scan rate allows many regions surrounding different domain nucleation centers inside the MCE sample to be active at the same time and not independent of each other. As for Appendix A, each of these regions contributes to developing the phase-boundary interface with a portion of surface having area A_i, and it affects the sample temperature T within a volume λ^3 around the nucleation center. However, the main difference with respect to the case of a thermal reservoir kept at a constant temperature T_b treated in Appendix A is represented by the fact that many irreversible events i, with each one associated with the motion of a single piece of surface A_i, occur concurrently within the volume λ^3. This circumstance happens because the heat provided by the reservoir at high scan rates is high enough to balance the change in temperature occurring in the λ^3 volume because of the phase-boundary motion, so the threshold temperatures T_{ci} and T_{hi} (see Sec. II B) are overcome almost simultaneously by many nucleation centers. Then all of the terms proportional to A_i appearing in the sum on the right-hand side of Eq. (16) must be taken into account and, since the damping coefficient α_s, the typical size λ, and the transition temperature T_t are the same for all of the events, we can write the area of the phase-boundary interface as $A = \sum_i A_i = \sum_i \ell_i^2$ (see also Sec. III A). The time constant related to the damping mechanism associated with the motion of the whole surface A is, in this case, denoted as τ_s, and it reads $\tau_s = \lambda^3 c_s/(\alpha_s \sum_i \ell i^2) = (\sum_i 1/\tau_{si})^{-1}$, where τ_{si} is the time constant, defined in Sec. III C, which refers to the damping of only a portion A_i of the whole boundary interface. It is worth noting that, depending on the upper limit in the previous sum, it can be either $A_i \sim A$ if the limit is low or $A_i \ll A$ if the limit is high enough. In the former case, we can assume that $\tau_s \sim \tau_{si} = \lambda^3 c_s/(\alpha_s \ell_i^2)$, while, in the latter case, we have $\tau_s \ll \tau_{si}$. More important, although $A_i \ll \lambda^2$, since we are assuming $\ell_i \ll \lambda$, it may happen that A, being the sum of many A_i's, will be greater than λ^2, so that also $\tau_c > \tau_s$. Hence, with respect to the constant T_b case, in the fast-scan-rate regime, there is also the possibility that the heat exchanged between the MCE sample and the external thermal reservoir may be primarily governed by the thermal contact details instead of the intrinsic kinetics of the phase transition.

From the experimental point of view, the heat-flux signal $q_s(t)$ detected in this regime is no longer characterized by individual peaks well separated in time associated with the different events i, as it is for the case of a constant T_b, but it rather shows a continuous behavior due to the superposition of many concurrent events. It is worth noting that, in this case also, the times t_i and t_f at which the phase transition begins and ends, respectively, identify the length in time of the whole heat-flux signal composed of many superimposed avalanches and not merely the time span of an individual single avalanche, as it is in Sec. III C and Appendix A. Moreover, the shape of q_s is also highly affected by the magnetic field H, which plays a prominent role here, since it determines the number of irreversible events i occurring in the sample at the same time. Indeed, as discussed in Appendix A, while H is approaching the critical value H_c, the temperature hysteresis ΔT^{hyst} is reduced, and thus the number of active regions in which new domains nucleate and grow is increased. This also means that the number of terms contributing to the sum appearing in Eq. (16) is increased, and this fact is reflected by the behavior of the sample temperature $T(t)$ and the heat-flux signal $q_s(t)$.

To solve Eqs. (17) and (18) in the case of a thermal-bath temperature varying in time as $T_b(t) = T_b(t_i) + \dot{T}_b(t - t_i)$ for $t > t_i$, with $\dot{T}_b > 0$ in a heating process or $\dot{T}_b < 0$ in a cooling case, we must first determine the initial value $T_b(t_i)$. To this aim, we observe that, before the transition starts, i.e., for $t \le t_i$, the sample temperature T has a small leg behind T_b due to the contact resistance $t_c/(\kappa_c A_c)$ between the MCE sample and the reservoir. Then we can conclude that $T_b(t) = T(t) + \tau_c \dot{T}_b$ for $t \le t_i$. At $t = t_i$, the sample temperature reaches the threshold value $T(t_i) = T_h$ in a heating process or $T(t_i) = T_c$ in the cooling case, so the initial condition on T_b reads $T_b(t_i) = T_h + \tau_c \dot{T}_b$ in heating and $T_b(t_i) = T_c + \tau_c \dot{T}_b = T_c - \tau_c |\dot{T}_b|$ in cooling.

With the above conditions and the time constant τ_{sc} defined as in Eqs. (A1), (A2), and (A3) but with τ_{si} replaced, in this case, by τ_s, the solution $T(t)$ of Eqs. (17) and (18) and the heat flux $q_s(t)$ read

$$T(t) = \begin{cases} T(t_i) + \frac{\tau_s}{\tau_c+\tau_s}\dot{T}_b(t-t_i) \mp \frac{\tau_c}{\tau_c+\tau_s}\left(\frac{\Delta T^{\text{hyst}}}{2} - \tau_{sc}|\dot{T}_b|\right)\left(1 - e^{-[(t-t_i)/\tau_{sc}]}\right), & \text{for } t_i \le t \le t_f, \\ T(t_i) - [T(t_i) - T(t_f)]e^{-[(t-t_f)/\tau_c]} + \dot{T}_b(t_f - t_i)\left(1 - e^{-[(t-t_f)/\tau_c]}\right) + \dot{T}_b(t - t_f), & \text{for } t > t_f, \end{cases} \tag{B1}$$

$$q_s(t) = \begin{cases} \pm\frac{\lambda^3 c_s}{\tau_c}\left[\tau_c|\dot{T}_b| + \frac{\tau_c}{\tau_c+\tau_s}|\dot{T}_b|(t-t_i) + \frac{\tau_c}{\tau_c+\tau_s}\left(\frac{\Delta T^{\text{hyst}}}{2} - \tau_{sc}|\dot{T}_b|\right)\left(1 - e^{-[(t-t_i)/\tau_{sc}]}\right)\right], & \text{for } t_i \le t \le t_f, \\ q_s(t_f)e^{-[(t-t_f)/\tau_c]} + \lambda^3 c_s \dot{T}_b\left(1 - e^{-[(t-t_f)/\tau_c]}\right), & \text{for } t > t_f, \end{cases} \tag{B2}$$

where the minus sign in Eq. (B1) and the plus sign in Eq. (B2) hold in heating, while the opposite signs in the same equations hold for cooling. Moreover, in analogy with Appendix A, we set $\Delta T^{\rm hyst} = T_h - T_c$ and $\Delta T^{\rm hyst}/2 = T_h - T_t = T_t - T_c$. Specifically, we observe that Eq. (B2) is evaluated by combining Eq. (B1) with Eqs. (8)–(15), following the same procedure used in Appendix A to obtain Eq. (A3). The heat current density $j_q(t)$, analogous to Eq. (A2), is simply obtained from Eq. (B2) as $j_q(t) = -q_s(t)/\lambda^2$.

There are two special limits of Eqs. (B1) and (B2) that deserve attention and allow us to simplify the above expressions, namely, the case in which the sample temperature $T(t)$ and the heat-flux signals q_s are far from their equilibrium values for the whole phase transition, a condition realized whenever $t_f - t_i \ll \tau_{sc}$, and, conversely, the case in which T and q_s can be close and can even reach the thermodynamic equilibrium during the transformation, i.e., $t_f - t_i \gtrsim \tau_{sc}$.

1. Far-from-equilibrium signals

When the signals are far from the thermodynamic equilibrium, the behavior of both $T(t)$ and $q_s(t)$ during the phase transition, i.e., for $t_i \le t \le t_f$, becomes linear in time, as it is for Eqs. (A1) and (A3), and it is given by

$$T(t) = T(t_i) + \dot{T}_b(t - t_i) \mp \frac{\Delta T^{\rm hyst}}{2\tau_s}(t - t_i), \quad \text{(B3)}$$

$$q_s(t) = \pm\lambda^3 c_s\left[|\dot{T}_b| + \frac{\Delta T^{\rm hyst}}{2\tau_c\tau_s}(t - t_i)\right], \quad \text{(B4)}$$

where in both equations we use the same convention on the signs as in Eqs. (B1) and (B2). Therefore, the far-from-equilibrium regime allows us to clearly distinguish the role played by the time constants τ_s and τ_c in determining the behavior of $T(t)$ and $q_s(t)$ during and after the phase transition. Indeed, as shown in Eq. (B3), the slope in the linear behavior of T during the phase transition is governed by the internal time constant τ_s only, independent of whether $\tau_c \ll \tau_s$ or, conversely, $\tau_c \gg \tau_s$. Concerning $q_s(t)$, Eq. (B4) shows, furthermore, that its linear behavior is characterized by a slope determined by both of the time constants τ_s and τ_c. When the transition is ended, i.e., for $t > t_f$, both T and q_s relax back to the thermodynamic equilibrium with an exponential law governed by τ_c only and described by Eqs. (B1) and (B2). The major difference with respect to the case of a constant T_b treated in Appendix A is that the behavior of both $T(t)$ and $q_s(t)$ depends now also on the constant rate $\dot{T}_b$. This fact is qualitatively depicted in Figs. 8 and 9, where the sample temperature T and the heat flux q_s are reported, upon heating, as a function of the thermal-bath temperature T_b at different rates $\dot{T}_b > 0$.

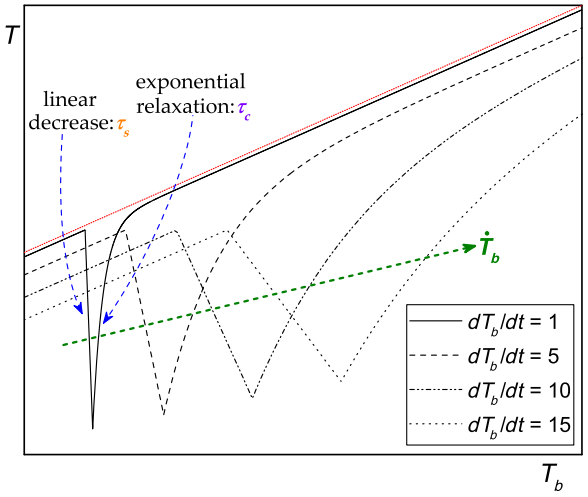

FIG. 8. Qualitative behavior of T vs T_b for far-from-equilibrium signals at different rates $\dot{T}_b = dT_b/dt > 0$, using Eq. (B3) for the linear decrease and Eq. (B1) (second row) for the exponential relaxation. The dotted red line shows the temperature T_b. $\dot{T}_b$ values in the legend are expressed in arbitrary units.

2. Close-to-equilibrium signals

The case of signals that can be close to or may even reach the thermodynamic equilibrium arises, interestingly, when the applied magnetic field H approaches the critical point H_c. Indeed, for $H \simeq H_c$, we have already noted that $\tau_c > \tau_s$, so that also $\tau_{sc} \simeq \tau_s$, because τ_{sc} is the parallel between τ_c and τ_s. Since, in this case, we have also pointed out that $\tau_s \ll \tau_{si}$ and we know from the experimental results reported in Sec. IV that $\tau_{si} = \lambda^3 c_s R_{si} = C_s R_{si}$ is on the order of 10–100 ms, we may suppose that the heat-flux

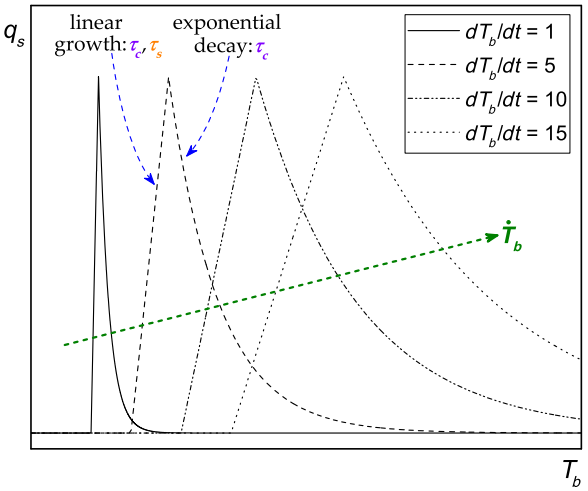

FIG. 9. Qualitative behavior of q_s vs T_b for far-from-equilibrium signals at different rates $\dot{T}_b = dT_b/dt > 0$, using Eq. (B4) for the linear growth and Eq. (B2) (second row) for the exponential decay. A constant offset $\lambda^3 c_s \dot{T}_b$ is subtracted from all of the curves. For the values in the legend, see Fig. 8.

signals last in times more than τ_s, i.e., $t_f - t_i \gtrsim \tau_{sc} \simeq \tau_s$. The linear approximation derived for the far-from-equilibrium signal regime no longer holds, but we can also, in this case, simplify Eqs. (B1) and (B2), noting that τ_s is now negligible with respect to τ_c. Then we obtain

$$T(t) = \begin{cases} T(t_i) \mp \frac{\Delta T^{\text{hyst}}}{2}(1 - e^{-[(t-t_i)/\tau_s]}) \pm \tau_s|\dot{T}_b|(1 - e^{-[(t-t_i)/\tau_s]} + \frac{t-t_i}{\tau_c}), & \text{for } t_i \le t \le t_f, \\ T(t_i) - [T(t_i) - T(t_f)]e^{-[(t-t_f)/\tau_c]} + \dot{T}_b(t_f - t_i)(1 - e^{-[(t-t_f)/\tau_c]}) + \dot{T}_b(t - t_f), & \text{for } t > t_f, \end{cases} \tag{B5}$$

$$q_s(t) = \begin{cases} \pm\lambda^3 c_s[|\dot{T}_b| + \frac{\Delta T^{\text{hyst}}}{2\tau_c}(1 - e^{-[(t-t_i)/\tau_s]}) + |\dot{T}_b|\frac{t-t_i}{\tau_c} - \frac{\tau_s}{\tau_c}|\dot{T}_b|(1 - e^{-[(t-t_i)/\tau_s]})], & \text{for } t_i \le t \le t_f, \\ q_s(t_f)e^{-[(t-t_f)/\tau_c]} + \lambda^3 c_s\dot{T}_b(1 - e^{-[(t-t_f)/\tau_c]}), & \text{for } t > t_f. \end{cases} \tag{B6}$$

We note from Eqs. (B5) and (B6) that $T(t)$ and $q_s(t)$ show, in this regime, an exponential behavior both during and after the transition, governed by τ_s and τ_c separately. Even in this case, Eqs. (B5) and (B6) can be linearized as a function of the thermal reservoir temperature $T_b(t)$—if the time constant τ_s is small enough—so that we can consider $t - t_i \gg \tau_s$ and we can safely neglect the exponentials appearing in these equations for $t_i \le t \le t_f$. Then the solutions describing the temperature and heat-flux behavior as a function of $T_b(t)$ during the phase transition, i.e., for $t_i \le t \le t_f$, read

$$T \simeq \frac{\tau_s}{\tau_c}T_b + T_t - \frac{\tau_s}{\tau_c}T(t_i) \simeq T_t, \tag{B7}$$

$$q_s \simeq \frac{\lambda^3 c_s}{\tau_c}(T_b - T_t). \tag{B8}$$

The most important feature encompassed in Eq. (B8) is represented by the fact that the heat flux q_s has a linear dependence on the thermal-bath temperature T_b characterized by a slope which is not dependent on the rate $\dot{T}_b$.

Similar linear behavior is shown, but as a function of the time t, at times well beyond the end of the transition, i.e., at $t \gg t_f$. In this case, the time behavior of T and q_s again becomes linear, as it is for $t \le t_i$ before the transition starts, and it is given by $T(t) = T_b(t) - [T(t_i) - T(t_f) + \dot{T}_b(t_f - t_i)]e^{-[(t-t_f)/\tau_c]} - \tau_c\dot{T}_b \simeq T_b(t) - \tau_c\dot{T}_b$ and $q_s(t) = \lambda^3 c_s[T_b(t) - T(t)]/\tau_c = \lambda^3 c_s\dot{T}_b$.

[1] O. Gutfleisch, M. A. Willard, E. Brück, C. H. Chen, S. G. Sankar, and J. Ping Liu, Magnetic materials and devices for the 21st century: Stronger, lighter, and more energy efficient, Adv. Mater. **23**, 821 (2011).

[2] K. G. Sandeman, Magnetocaloric materials: The search for new systems, Scr. Mater. **67**, 566 (2012).

[3] I. Takeuchi and K. Sandeman, Solid-state cooling with caloric materials, Phys. Today **68**, No. 12, 48 (2015).

[4] A. Kitanovski, J. Tušek, U. Tomc, U. Plaznik, M. Ozbolt, and A. Poredoš, *Magnetocaloric Energy Conversion—From Theory to Applications* (Springer International Publishing, Cham, Switzerland, 2015).

[5] J. Lyubina, Magnetocaloric materials for energy efficient cooling, J. Phys. D **50**, 053002 (2017).

[6] P. Debye, Some remarks on magnetization at low temperature, Ann. Phys. (Berlin) **386**, 1154 (1926).

[7] W. F. Giauque, A thermodynamic treatment of certain magnetic effects. A proposed method of producing temperatures considerably below 1° absolute, J. Am. Chem. Soc. **49**, 1864 (1927).

[8] K. A. Gschneidner, Jr., V. K. Pecharsky, and A. O. Tsokol, Recent developments in magnetocaloric materials, Rep. Prog. Phys. **68**, 1479 (2005).

[9] E. Brück, O. Tegus, D. T. Cam Thanh, N. T. Trung, and K. H. J. Buschow, A review on Mn based materials for magnetic refrigeration: Structure and properties, Int. J. Refrig. **31**, 763 (2008).

[10] B. G. Shen, J. R. Sun, F. X. Hu, H. W. Zhang, and Z. H. Cheng, Recent progress in exploring magnetocaloric materials, Adv. Mater. **21**, 4545 (2009).

[11] R. Caballero-Flores, V. Franco, A. Conde, K. E. Knipling, and M. A. Willard, Optimization of the refrigerant capacity in multiphase magnetocaloric materials, Appl. Phys. Lett. **98**, 102505 (2011).

[12] V. Franco, J. S. Blázquez, B. Ingale, and A. Conde, The magnetocaloric effect and magnetic refrigeration near room temperature: Materials and models, Annu. Rev. Mater. Res. **42**, 305 (2012).

[13] A. Smith, C. R. H. Bahl, R. Bjørk, K. Engelbrecht, K. K. Nielsen, and N. Pryds, Materials challenges for high performance magnetocaloric refrigeration devices, Adv. Energy Mater. **2**, 1288 (2012).

[14] A Smaïli and R. Chahine, Thermodynamic investigations of optimum active magnetic regenerators, Cryogenics **38**, 247 (1998).

[15] A. Sarlah, A. Kitanovski, A. Poredos, P. W. Egolf, O. Sari, F. Gendre, and Ch. Besson, Static and rotating active magnetic regenerators with porous heat exchangers for magnetic cooling, Int. J. Refrig. **29**, 1332 (2006).

[16] J. B. Jensen, K. Engelbrecht, C. R. H. Bahl, N. Pryds, G. F. Nellis, S. A. Klein, and B. Elmegaard, Modeling of

parallel-plate regenerators with non-uniform plate distributions, Int. J. Heat Mass Transfer **53**, 5065 (2010).

[17] J. B. Jensen, C. R. H. Bahl, K. Engelbrecht, B. Elmegaard, and N. Pryds, Analysis of single blow effectiveness in non-uniform parallel plate regenerators, Int. J. Heat Mass Transfer **54**, 4746 (2011).

[18] C. R. H. Bahl, K. Engelbrecht, R. Bjørk, D. Eriksen, A. Smith, K. K. Nielsen, and N. Pryds, Design concepts for a continuously rotating active magnetic regenerator, Int. J. Refrig. **34**, 1792 (2011).

[19] K. Engelbrecht, K. K. Nielsen, and N. Pryds, An experimental study of passive regenerator geometries, Int. J. Refrig. **34**, 1817 (2011).

[20] L. Theil Kuhn, N. Pryds, C. R. H. Bahl, and A. Smith, Magnetic refrigeration at room temperature—From magnetocaloric materials to a prototype, J. Phys. Conf. Ser. **303**, 012082 (2011).

[21] K. K. Nielsen, K. Engelbrecht, D. V. Christensen, J. B. Jensen, A. Smith, and C. R. H. Bahl, Degradation of the performance of microchannel heat exchangers due to flow maldistribution, Appl. Therm. Eng. **40**, 236 (2012).

[22] K. K. Nielsen, K. Engelbrecht, and C. R. H. Bahl, The influence of flow maldistribution on the performance of inhomogeneous parallel plate heat exchangers, Int. J. Heat Mass Transfer **60**, 432 (2013).

[23] Z. Chen, Y. Utaka, and Y. Tasaki, Measurement and numerical simulation on the heat transfer characteristics of reciprocating flow in microchannels for the application in magnetic refrigeration, Appl. Therm. Eng. **65**, 150 (2014).

[24] Y. Kotani, Y. Kansha, M. Ishizuka, and A. Tsutsumi, Experimental investigation of an active magnetic regenerative heat circulator applied to self-heat recuperation technology, Appl. Therm. Eng. **70**, 1202 (2014).

[25] J. A. Lozano, K. Engelbrecht, C. R. H. Bahl, K. K. Nielsen, J. R. Barbosa, Jr., A. T. Prata, and N. Pryds, Experimental and numerical results of a high frequency rotating active magnetic refrigerator, Int. J. Refrig. **37**, 92 (2014).

[26] D. S. Arnold, A. Tura, A. Ruebsaat-Trott, and A. Rowe, Design improvements of a permanent magnet active magnetic refrigerator, Int. J. Refrig. **37**, 99 (2014).

[27] A. Kitanovski, U. Plaznik, U. Tomc, and A. Poredoš, Present and future caloric refrigeration and heat-pump technologies, Int. J. Refrig. **57**, 288 (2015).

[28] J. E. Cararo, J. A. Lozano, P. V. Trevizoli, R. Teyber, A. Rowe, and J. R. Barbosa, Jr., in *Proceedings of the 7th International Conference on Magnetic Refrigeration at Room Temperature (Thermag VII), Turin, 2016* (International Institute of Refrigeration, Paris, 2016), p. 115.

[29] B. Monfared and B. Palm, in *Proceedings of the 7th International Conference on Magnetic Refrigeration at Room Temperature (Thermag VII), Turin, 2016* (International Institute of Refrigeration, Paris, 2016), p. 146.

[30] H. N. Bez, K. Navickaite, T. Lei, K. Engelbrecht, A. Barcza, and C. R. H. Bahl, in *Proceedings of the 7th International Conference on Magnetic Refrigeration at Room Temperature (Thermag VII), Turin, 2016* (International Institute of Refrigeration, Paris, 2016), p. 158.

[31] F. Scarpa, L. A. Tagliafico, and M. Gigante, in *Proceedings of the 7th International Conference on Magnetic Refrigeration at Room Temperature (Thermag VII), Turin, 2016* (International Institute of Refrigeration, Paris, 2016), p. 303.

[32] R. Teyber, P. V. Trevizoli, T. V. Christiaanse, P. Govindappa, I. Niknia, and A. Rowe, Performance evaluation of two-layer active magnetic regenerators with second-order magnetocaloric materials, Appl. Therm. Eng. **106**, 405 (2016).

[33] M. D. Kuz'min, Factors limiting the operation frequency of magnetic refrigerators, Appl. Phys. Lett. **90**, 251916 (2007).

[34] P.-W. Ma and S. L. Dudarev, Dynamic magnetocaloric effect in bcc iron and hcp gadolinium, Phys. Rev. B **90**, 024425 (2014).

[35] A. M. Aliev, A. B. Batdalov, L. N. Khanov, V. V. Koledov, V. G. Shavrov, I. S. Tereshina, and S. V. Taskaev, Magnetocaloric effect in some magnetic materials in alternating magnetic fields up to 22 Hz, J. Alloys Compd. **676**, 601 (2016).

[36] A. Fujita, S. Fujieda, Y. Hasegawa, and K. Fukamichi, Itinerant-electron metamagnetic transition and large magnetocaloric effects in $La(Fe_xSi_{1-x})_{13}$ compounds and their hydrides, Phys. Rev. B **67**, 104416 (2003).

[37] O. Tegus, E. Brück, K. H. J. Buschow, and F. R. de Boer, Transition-metal-based magnetic refrigerants for room-temperature applications, Nature (London) **415**, 150 (2002).

[38] V. K. Pecharsky and K. A. Gschneidner, Jr., Giant Magnetocaloric Effect in $Gd_5(Si_2Ge_2)$, Phys. Rev. Lett. **78**, 4494 (1997).

[39] J. D. Moore, K. Morrison, K. G. Sandeman, M. Katter, and L. F. Cohen, Reducing extrinsic hysteresis in first-order $La(Fe, Co, Si)_{13}$ magnetocaloric systems, Appl. Phys. Lett. **95**, 252504 (2009).

[40] K. Morrison, J. D. Moore, K. G. Sandeman, A. D. Caplin, and L. F. Cohen, Capturing first- and second-order behavior in magnetocaloric $CoMnSi_{0.92}Ge_{0.08}$, Phys. Rev. B **79**, 134408 (2009).

[41] K. Morrison, J. Lyubina, J. D. Moore, A. D. Caplin, K. G. Sandeman, O. Gutfleisch, and L. F. Cohen, Contributions to the entropy change in melt-spun $LaFe_{11.6}Si_{1.4}$, J. Phys. D **43**, 132001 (2010).

[42] K. Morrison, M. Bratko, J. Turcaud, A. Berenov, A. D. Caplin, and L. F. Cohen, A calorimetric method to detect a weak or distributed latent heat contribution at first order magnetic transitions, Rev. Sci. Instrum. **83**, 033901 (2012).

[43] E. Lovell, A. M. Pereira, A. D. Caplin, J. Lyubina, and L. F. Cohen, Dynamics of the first-order metamagnetic transition in magnetocaloric $La(Fe, Si)_{13}$: Reducing hysteresis, Adv. Energy Mater. **5**, 1401639 (2015).

[44] E. Lovell, M. Bratko, A. D. Caplin, A. Barzca, M. Katter, L. Ghivelder, and L. F. Cohen, Magnetic relaxation dynamics driven by the first-order character of magnetocaloric $La(Fe, Mn, Si)_{13}$, Phil. Trans. R. Soc. A **374**, 20150307 (2016).

[45] O. Gutfleisch, T. Gottschall, M. Fries, D. Benke, I. Radulov, K. P. Skokov, H. Wende, M. Gruner, M. Acet, P. Entel, and M. Farle, Mastering hysteresis in magnetocaloric materials, Phil. Trans. R. Soc. A **374**, 20150308 (2016).

[46] L. Ghivelder, G. G. Eslava, R. S. Freitas, G. Leyva, and F. Parisi, Avalanche-like metamagnetic transition in (LaNd) CaMnO manganites, J. Alloys Compd. **680**, 494 (2016).

[47] H. Yako, S. Fujieda, A. Fujita, and K. Fukamichi, Influence of demagnetizing effect on the kinetics of the itinerant

electron metamagnetic transition in magnetic refrigerant $La(Fe_{0.88}Si_{0.12})_{13}$, IEEE Trans. Magn. **47**, 2482 (2011).

[48] A. Fujita and H. Yako, Kinetics of thermally induced first-order magnetic transition in $La(Fe_{0.88}Si_{0.12})_{13}$ itinerant electron metamagnet, J. Alloys Compd. **577S**, S48 (2013).

[49] A. Fujita, T. Kondo, M. Kano, and H. Yako, Shape-anisotropic heterogeneous nucleation and magnetic Gibbs-Thomson effect in itinerant-electron metamagnetic transition of $La(Fe_{0.88}Si_{0.12})_{13}$ magnetocaloric compound, Appl. Phys. Lett. **102**, 041913 (2013).

[50] M. Kuepferling, C. P. Sasso, and V. Basso, Rate dependence of the magnetocaloric effect in La-Fe-Si compounds, EPJ Web Conf. **40**, 06010 (2013).

[51] M. Kuepferling, C. Bennati, F. Laviano, G. Ghigo, and V. Basso, Dynamics of the magneto structural phase transition in $La(Fe_{0.9}Co_{0.015}Si_{0.085})_{13}$ observed by magneto-optical imaging, J. Appl. Phys. **115**, 17A925 (2014).

[52] W. A. Johnson and R. F. Mehl, Reaction kinetics in processes of nucleation and growth, Trans. Am. Inst. Min. Metall. Eng. **135**, 416 (1939).

[53] M. Avrami, Kinetics of phase change. I General theory, J. Chem. Phys. **7**, 1103 (1939); Kinetics of phase change. II Transformation—Time relations for random distribution of nuclei, J. Chem. Phys. **8**, 212 (1940); Granulation, phase change, and microstructure. Kinetics of phase change. III, J. Chem. Phys. **9**, 177 (1941).

[54] C. Bennati, L. Gozzelino, E. S. Olivetti, and V. Basso, Heterogeneous nucleation and heat flux avalanches in $La(Fe, Si)_{13}$ magnetocaloric compounds near the critical point, Appl. Phys. Lett. **109**, 231904 (2016).

[55] L. P. Kadanoff, S. R. Nagel, L. Wu, and S.-m. Zhou, Scaling and universality in avalanches, Phys. Rev. A **39**, 6524 (1989).

[56] E. K. H. Salje and K. A. Dahmen, Crackling noise in disordered materials, Annu. Rev. Condens. Matter Phys. **5**, 233 (2014).

[57] F. Casanova, A. Labarta, X. Batlle, E. Vives, J. Marcos, L. Mañosa, and A. Planes, Dynamics of the first-order magnetostructural transition in $Gd_5(Si_xGe_{1-x})_4$, Eur. Phys. J. B **40**, 427 (2004).

[58] B. Ludwig, C. Strothkaemper, U. Klemradt, X. Moya, L. Mañosa, E. Vives, and A. Planes, Premartensitic transition in Ni_2MnGa Heusler alloys: Acoustic emission study, Phys. Rev. B **80**, 144102 (2009).

[59] G. Bertotti, *Hysteresis in Magnetism* (Academic Press, Boston, 1998).

[60] *The Science of Hysteresis*, Vol. II, edited by G. Bertotti and I. D. Mayergoyz (Academic Press, Oxford, 2006).

[61] M. Ghorbani Zavareh, C. Salazar Mejía, A. K. Nayak, Y. Skourski, J. Wosnitza, C. Felser, and M. Nicklas, Direct measurements of the magnetocaloric effect in pulsed magnetic fields: The example of the Heusler alloy $Ni_{50}Mn_{35}In_{15}$, Appl. Phys. Lett. **106**, 071904 (2015).

[62] F. Cugini, G. Porcari, C. Viappiani, L. Caron, A. O. dos Santos, L. P. Cardoso, E. C. Passamani, J. R. C. Proveti, S. Gama, E. Brück, and M. Solzi, Millisecond direct measurement of the magnetocaloric effect of a Fe_2P-based compound by the mirage effect, Appl. Phys. Lett. **108**, 012407 (2016).

[63] L. I. Rubinstein, *The Stefan Problem* (American Mathematical Society, Providence, 1971).

[64] V. Alexiades and A. D. Solomon, *Mathematical Modeling of Melting and Freezing Processes* (Hemisphere Publishing, Washington, DC, 1993).

[65] S. C. Gupta, *The Classical Stefan Problem: Basic Concepts, Modelling and Analysis*, 1st ed. (Elsevier Science, Amsterdam, 2003).

[66] A. Visintin, *Models of Phase Transitions* (Birkhäuser, Boston, 1996).

[67] H. B. Callen, *Thermodynamics and an Introduction to Thermostatistics*, 2nd ed. (John Wiley & Sons, New York, 1985).

[68] J. Crank, *Free and Moving Boundary Problems* (Clarendon Press, Oxford, 1984).

[69] M. E. Glicksman, *Principles of Solidification—An Introduction to Modern Casting and Crystal Growth Concepts* (Springer-Verlag, New York, 2011).

[70] M. J. O'Neill, The analysis of a temperature-controlled scanning calorimeter, Anal. Chem. **36**, 1238 (1964).

[71] V. Basso, C. P. Sasso, and M. Küpferling, A Peltier cells differential calorimeter with kinetic correction for the measurement of $c_p(H,T)$ and $\Delta s(H,T)$ of magnetocaloric materials, Rev. Sci. Instrum. **81**, 113904 (2010).

[72] V. Basso, M. Küpferling, C. Curcio, C. Bennati, A. Barzca, M. Katter, M. Bratko, E. Lovell, J. Turcaud, and L. F. Cohen, Specific heat and entropy change at the first order phase transition of $La(Fe\text{-}Mn\text{-}Si)_{13}$-H compounds, J. Appl. Phys. **118**, 053907 (2015).

[73] D. S. Fisher, Scaling and Critical Slowing Down in Random-Field Ising Systems, Phys. Rev. Lett. **56**, 416 (1986).

[74] C. Djurberg, P. Svedlindh, P. Nordblad, M. F. Hansen, F. Bødker, and S. Mørup, Dynamics of an Interacting Particle System: Evidence of Critical Slowing Down, Phys. Rev. Lett. **79**, 5154 (1997).